

FEDSM-ICNMM2010-30159

MODERATE REYNOLDS NUMBER MIXING IN A T-CHANNEL

Susan Thomas

Department of Mechanical Engineering
University of Utah
Salt Lake City, Utah 84112
Email: thomas.susank@gmail.com

Tim Ameal

Department of Mechanical Engineering
University of Utah
Salt Lake City, Utah 84112
Email: ameel@mech.utah.edu

ABSTRACT

An experimental investigation of water flow in a T-shaped channel with rectangular cross section (20 x 20 mm inlet ID and 20 x 40 mm outlet ID) has been conducted for a Reynolds number Re range of 56 to 422, based on inlet diameter. Dynamical conditions and the T-channel geometry of the current study are applicable to the microscale. This study supports a large body of numerical work, and resolution and the interrogation region are extended beyond previous experimental studies. Laser induced fluorescence (LIF) and particle imaging velocimetry (PIV) are used to characterize flow behaviors over the broad range of Re where realistic T-channels operate. Scalar structures previously unresolved in the literature are presented. Special attention is paid to the unsteady flow regimes that develop at moderate Re , which significantly impact mixing but are not yet well characterized or understood. An unsteady symmetric topology, which develops at higher Re and negatively impacts mixing, is presented, and mechanisms behind the wide range of mixing qualities predicted for this regime are explained. An optimal Re operating range is identified based on multiple experimental trials.

INTRODUCTION

Microscale fluid mixing applies to lab-on-a-chip analytical microfluidic devices and drug delivery systems [1–3], miniaturized turbines, engines, and chemical reactors [4–6], and electronic chip cooling [7]. Despite challenges such as high pressure drops, high surface-to-volume ratios, and limited fabrication techniques [8–11], effective mixing has been achieved in laboratory settings with active mixing mechanisms such as pulsed electromagnetic fields and integrated pumps and valves, [12–14] and complex microgeometries that promote flow reorientation and lamination [15–20]. Fabricating these clever micromixers can be undesirably complex.

A simple T-channel geometry, with square inlet ports of hydraulic diameter d and a rectangular outlet port of height d and

width $2d$, is attractive because it is easy to fabricate, can facilitate high- and low-throughput mixing, and, when built on a chip, permits fabrication of on chip-reservoirs or the attachment of macroscale tubing, as a T-shaped geometry provides maximum separation of inlet/outlet ports. Multiple numerical simulations have predicted that a T-channel is also capable of effective mixing when an asymmetric two-vortex flow regime, identified from the planar topology in the T-channel junction and denoted engulfment flow in the initial work of Kockmann *et al.* [21], occurs at moderate Re . The numerical work of Kockmann *et al.* [21] has generally identified an engulfment flow regime for $188 \leq Re \leq 233$, where Re is the Reynolds number based on the inlet hydraulic diameter.

Experimental characterizations of T-channel mixing have been limited by challenges associated with microflow interrogation, and measurements to date have been largely non-local. Engler *et al.* [22] used integral measurements of inlet and outlet pressure to estimate the onset of engulfment flow based on a sharp rise in pressure drop. Their results suggested a geometry-dependent Re range (broader by approximately 30% when compared to the numerical predictions of [21]) for the onset of engulfment flow. Kockmann *et al.* [23] computed a volumetric measure of mixing from dye concentration measurements at the outlet, and found a continual increase in mixing quality with increasing Re for moderate Reynolds numbers, and a near-constant mixing quality at higher Reynolds numbers. Both Wong *et al.* [24] and Engler *et al.* [22] used dye-visualization techniques to visualize engulfment flow in the outlet channel from a top-wise vantage point. Local flow structure was not resolved.

The recent numerical publications of Hoffmann *et al.* [25] and Bothe *et al.* [26] considered the impact of chemical reaction on mixing quality at the outlet. In 2009, the existence of unsteady flows at moderate Re was predicted in computational fluid dynamics (CFD) simulations by Dreyer [27] *et al.* Unsteady regimes have not yet been experimentally characterized, and the need for good experimental data was stressed in [27]. The primary goals of this study

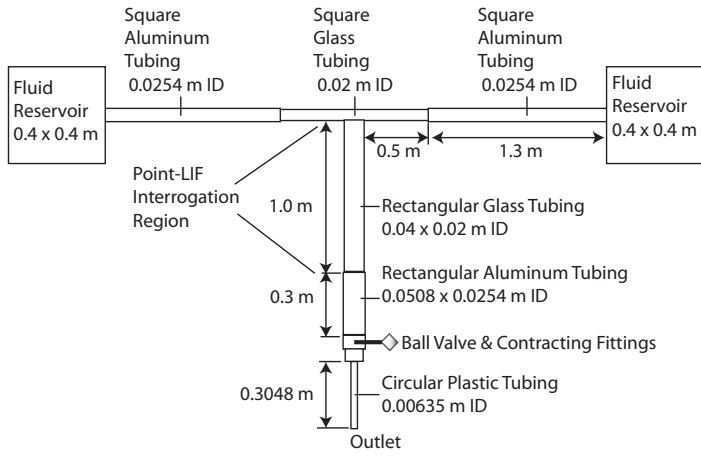


FIGURE 1. Schematic of the symmetric T-channel apparatus, top view.

are to provide such data, and to describe both steady and unsteady behaviors with whole-field and discrete point interrogations that are temporally and spatially resolved beyond what is currently available in the literature. Additionally, this paper seeks to elucidate numerically predicted mixing trends on a fundamental level, to include an examination of scalar structures that have previously been numerically (due to numerical diffusion in [25–27]) and experimentally unresolved.

EXPERIMENTAL APPARATUS

A T-channel test section was fabricated using two 1.22 m long sections of rectangular glass tubing of 20 x 20 mm ID (inlet channels), and 20 x 40 mm ID (outlet channel). To affix these together in a T-configuration, an opening was machined mid-length into the sidewall of the smaller channel. Glass tubes were miter-fit to ensure a smooth T-channel connection and sealed with silicon. The glass T-channel was solidly affixed to stiff aluminite backing, and then to a specially constructed aluminum table. Inlet glass tubing was joined to 25.4 mm ID square aluminum tubing on each side of the junction for a total inlet-to-inlet length of 3.66 m. Leveled gravity-fed inlet tanks of 40.64 x 40.64 cm footprint and 36.48 cm depth were used to drive the flow. It is noted that 1) inlet lengths of the T-channel apparatus are sufficient to ensure that flow reaching the junction is fully-developed, 2) the T-channel apparatus was leveled over the length, with special care given to the T-junction such that it is locally level, and 3) symmetry between the inlets is maintained with equivalent tubing lengths and attachment fittings. A schematic of the T-channel apparatus is shown in Fig. 1. Flow rate was adjusted between trials by varying the height differential between the inlets and outlet.

MEASUREMENTS & DATA REDUCTION

LIF in the Outlet Channel

Planar LIF visualizations in the outlet channel mid-plane were used as a qualitative indicator of mixing behavior. The total interrogated area was 0.04 x 0.410 m, or the width of the outlet channel and a length of $\geq 20D$ downstream, where D is the hydraulic diameter of the inlet channels, $D = 20$ mm. A Coherent® brand con-

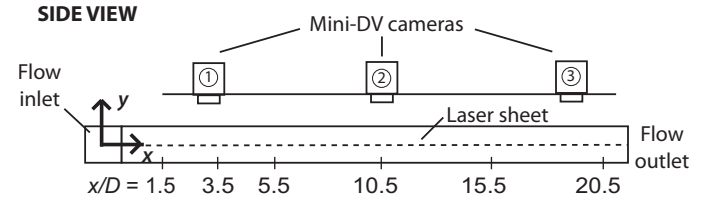


FIGURE 2. Schematic of the three-camera, planar LIF system in the T-channel outlet. Photodetector locations are indicated in the figure. Note that photodetector locations $x/D = 1.5, 3.5$, and 5.5 are within the viewing plane of camera 1, while $x/D = 10.5$, and $x/D = 15.5$ and 20.5 are captured by cameras 2 and 3, respectively.

tinuous argon-ion laser and a cylindrical lens were used to create a laser sheet. To record flow behavior in real time, three simultaneously employed high-resolution camcorders (30 Hz recording rate) were mounted atop the T-channel. A schematic of the LIF system is shown in Fig. 2. Note that coordinates $\langle xyz \rangle = \langle 000 \rangle$ mark the center point of the T-channel junction.

Spanwise concentration profiles were extracted from scalar concentration fields for downstream locations of $x/D = 1.5, 3.5, 5.5, 10.5$, and 15.5 . Dimensional concentration data were normalized by 1) subtracting average concentration profiles at each x/D location as determined from LIF images of a homogeneous, mean-concentration flow field, and 2) dividing the result by one-half of the difference between the concentration profiles at the same location for a homogeneous high-concentration and clear-fluid flow field. The resulting non-dimensional concentration profiles $c(z/D)$ vary from 1, when high concentration fluid is present, to -1, when clear fluid is present. Fast Fourier transforms (FFT's) of non-dimensional concentration profiles were performed to quantify the length scales associated with concentration distributions at each x/D location.

Combined Planar- and Point-LIF

Planar LIF in the T-channel junction was employed simultaneously with point-LIF at discrete outlet-channel locations of $x/D = 1.5, 3.5, 5.5, 10.5, 15.5$, and 20.5 to correlate the evolution of flow structure in the junction with downstream advective behavior. A schematic is shown in Fig. 3. Note that coordinates $\langle xyz \rangle = \langle 000 \rangle$ mark the center point of the T-channel junction. Point-LIF (Fig. 3) has three main experimental components: 1) photodetectors, which are sensitive rapid-response photodiode circuits that detect output intensity, 2) a longpass filter sandwiched between two identical plano-convex lenses to collect directed intensity from a discrete point within the channel while attenuating scattered light, and 3) beams of laser light, directed to x/D locations by fiber optics and (nearly) recollimated by integrated gradient index (GRIN) lenses, which illuminate the flow.

A Coherent® brand continuous argon-ion laser illuminated the flow, and a beam splitter (not shown in Fig. 3) facilitated simultaneous measurements by directing half of the output laser energy through a cylindrical lens to create the laser sheet for planar LIF, and the other half through the fiber optic bundle for point-LIF interrogations. A high-resolution camera recorded planar LIF visualizations in real time, and a LabView data acquisition system captured each photodetector response (a voltage signal) for point-LIF mea-

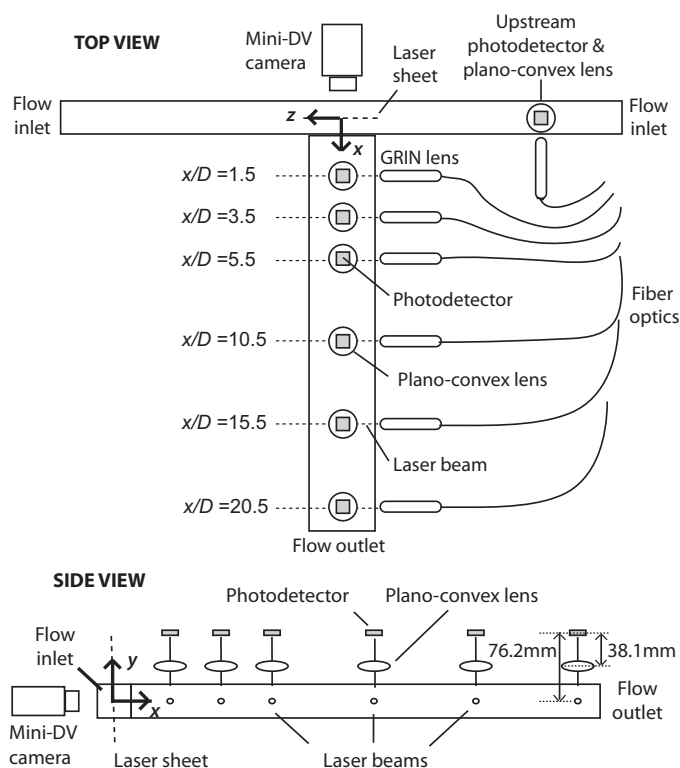


FIGURE 3. Schematic of simultaneous point-LIF in the outlet channel and planar-LIF in the T-channel junction, top and side view. Note that mounting distances above the channel for the longpass-filter/lens array correspond with the effective focal length of the plano-convex lenses.

surements. Uranine, in concentrations of $\approx 3 \text{ g/m}^3$, was added to a single inlet tank and served as the passive, fluorescing scalar. The Schmidt number Sc for uranine dye in water is $\sim 10^3$. Point-LIF voltage signals were conditioned by 1) subtracting an average output voltage as determined from calibration on a mid-concentration homogeneous flow field, and 2) dividing the result by one-half of the difference between voltages output for a homogeneous high-concentration and clear fluid flow field. The resulting signals represent scalar concentration in the channel centerline with time, $c(t)$, and vary between the limits of $c(t) = 1$ and $c(t) = -1$ for an interrogated volume of high-concentration and zero-concentration fluid, respectively.

PIV in Three Planes

Planar PIV was used at multiple locations in the T-channel junction and outlet channel to reveal the three-dimensional structure that impacts mixing. For PIV measurements, both inlet tanks were doped with $9 \mu\text{m}$ glass beads of specific gravity 1.04. A pulsed Newwave Nd:YAG-laser of 532 nm wavelength with integrated light-sheet optics was used to illuminate the flow. A charge coupled discharge (CCD) camera with a 32 Hz frame rate was used to image the flow. Vector fields were generated from raw PIV images. The PIV sampling rate was approximately 1 complete vector field per second. Machined hardware mounts were used to rigidly fix the camera, laser and T-channel orthogonally, and the 1.1 mm thick laser sheet was positioned with a linear stage system of 0.5 mm resolution. A schematic of PIV interrogation planes is shown

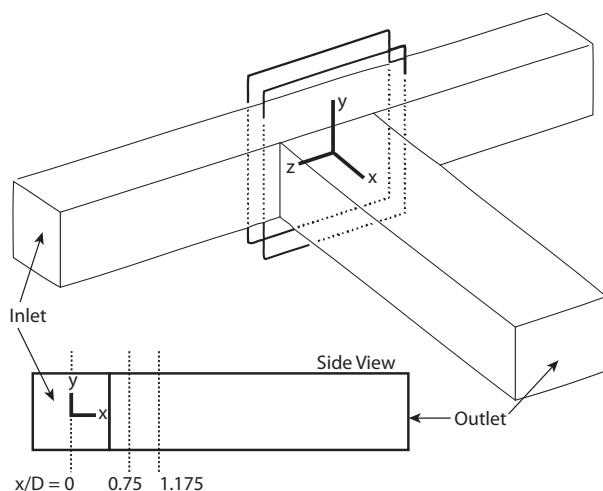


FIGURE 4. Schematic of PIV viewing planes at $x = 0, 15$, and 23.5 mm . $\langle xyz \rangle = \langle 000 \rangle$ is the junction centerpoint, and the vantage point is from the back of the T-mixer looking down the outlet channel.

in Fig. 4. Coordinates $\langle xyz \rangle = \langle 000 \rangle$ mark the centerpoint of the T-channel junction; positive x is in the outlet-channel direction. Note that for all PIV results, the viewing plane is from the backside of the mixer, as if looking down the T-channel outlet.

Mass Flow Rate

To compute the Reynolds number, mass flow rate was measured with a dynamic-weighting procedure (weight of fluid collected in a container over a measured time interval) at the outlet and halved to calculate an average Reynolds number in each channel. The dynamic-weighting method was chosen for its relatively low uncertainty and ability to accommodate a wide range of Re . Per hydrostatic equilibrium, tanks must maintain the same fluid height above the outlet, and the assumption of equivalent drain over a finite time interval is valid for two hydrodynamically connected tanks if: 1) inlet tanks are of equivalent cross-sectional area (A) so that changes in fluid volume (Q) are equivalent ($Q_1 = \Delta h_1 \times A_1 = \Delta h_2 \times A_2 = Q_2$), and 2) fluid properties and inlet channel dimensions on both sides of the junction are identical. In the present experiment, equivalency of inlet channel flow rates is expected, but was additionally verified with PIV measurements in both inlet channels. Time intervals were measured with a digital stopwatch. Averaging times for each flow rate were chosen such that the uncertainty in measured mass was $\leq 1\%$. Temperature was measured in the center of each inlet tank at the beginning and end of each trial to compute property values, and to ensure that constant and equivalent temperatures were maintained over the time period of each experimental trial (45 to 70 minutes). Total relative uncertainty in Re , considering temperature, channel dimensions, digital scale and timing uncertainties, was calculated as nominally 5.4%.

RESULTS AND DISCUSSION

Flow Regimes

Fig. 5a and Fig. 5b show symmetric and asymmetric topologies, respectively, that occur in the T-junction at low Re . Flows

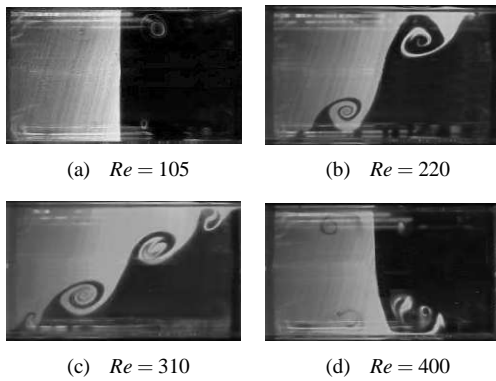


FIGURE 5. LIF images in the junction centerplane at $x/D = 0$ for (a) steady symmetric flow at low Re , (b) steady asymmetric flow, (c) unsteady asymmetric flow, and (d) unsteady symmetric flow at higher Re . Doped fluid enters from the left side.

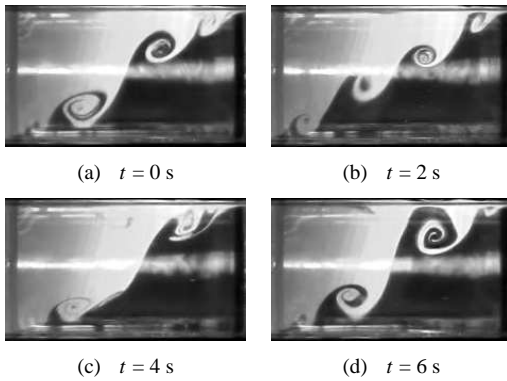


FIGURE 6. LIF still frames extracted in two-second intervals for unsteady asymmetric flow in the junction centerplane ($x = 0$) for $Re = 290$.

at the lowest Re are symmetric about $y, z = 0$ and include both stagnation-point flows (at the lowest Re) and the four-vortex flow shown in Fig. 5a. Flows at moderate Re , $Re \geq 135$ in this study, transition to the asymmetric, co-rotating two-vortex topology of Fig. 5b. Both regimes have been described in the literature [21–26]. LIF video indicates that symmetric and asymmetric flows at low Re (Fig. 5a and b) are perfectly stationary.

Unsteady asymmetric flow shown in Fig. 5c is characterized by a shear-layer like roll-up of the fluid interface in which repeating patterns of two and four vortices appear, roll along the unsteady interface, and annihilate. Time-sequenced LIF images of this process are shown in Fig. 6 for $Re = 290$. As indicated by Fig. 6, unsteady asymmetric flow in the T-channel junction is oscillatory, and two- and four-vortex topologies reoccur at regular intervals. Reynolds numbers between 190 and 240 marked the onset of unsteady asymmetric behavior in this study. Unsteady behaviors have been numerically predicted to occur for $Re \approx 180$ [26, 27].

At higher Re , there is a reemergence of symmetry in the junction, as shown in Fig. 5d. Flow in Fig. 5d is also periodic, as unstable stagnation streamlines at the top and bottom walls move alternately rightward and leftward about the vertical centerline. This behavior is most visible in Fig. 5d near the bottom wall, where dyed fluid has moved rightward across the vertical centerline to become

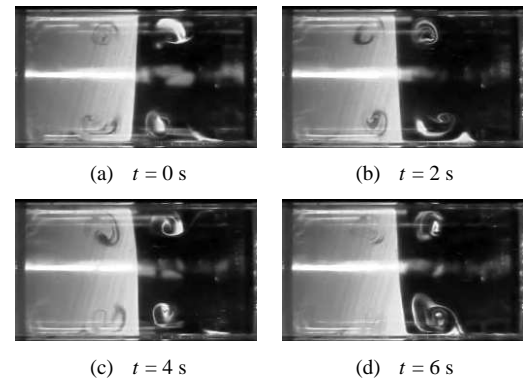


FIGURE 7. LIF still frames extracted in two-second intervals for unsteady asymmetric flow in the junction centerplane ($x = 0$) for $Re = 390$.

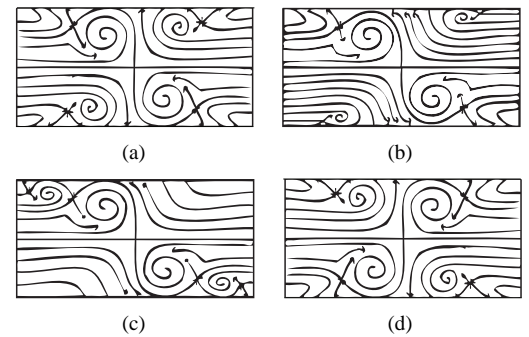


FIGURE 8. Schematic of unstable streamline oscillation for unsteady symmetric flow at higher Re .

entangled in the vortex in the lower right quadrant. Note that opposing motion, which is partially obscured by reflection, has simultaneously occurred at the top wall, where clear fluid has moved leftward across the vertical centerline to participate in the vortex in the top left quadrant. Time-sequenced LIF images of this process are shown Fig. 7.

The schematic in Fig. 8 depicts the near-wall reallocation of mass and momentum that occurs with unstable stagnation streamline oscillation. From Fig. 8a to b, an increasingly off-center stagnation streamline leads to greater disparity in vortex size and strength. Diminished vortex/saddle point pairs (upper right and lower left quadrants in a and b) move nearer to the wall, and, if sufficient momentum is redirected, disappear from the plane (Fig. 8c). Importantly, if small secondary vortices appear (upper left and lower right quadrant, Fig. 8c) and are sufficiently strong, movement to Fig. 8d, in which the cycle begins to repeat, will be delayed by the temporary transition to asymmetric shear-layer flow (as in Fig. 6). Hence, unpredictable breaks from symmetry occur as flows oscillate between rightward and leftward asymmetries, but a high-degree of symmetry on average persists. Unsteady symmetric flow occurred in this study for $Re \geq 335$.

A periodic four-vortex state was predicted in the numerical simulations of Telib *et al.* [28] for a T-shaped mixer with circular inlets, but has not yet been detailed in the literature for a square-channel T-mixer. Oscillatory behaviors, denoted periodic pulsating and quasi-periodic pulsating flow based on the reproducibility of

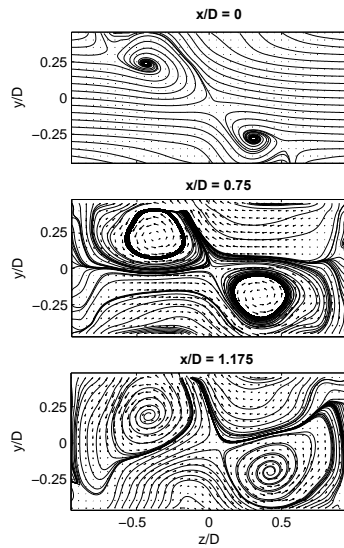


FIGURE 9. Time-averaged PIV vector fields and streamlines for asymmetric two-vortex flow in three viewing planes, $Re = 250$.

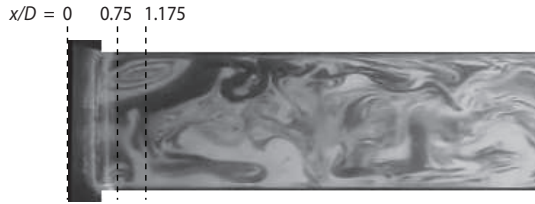


FIGURE 10. Instantaneous planar LIF image for unsteady asymmetric flow in the outlet channel centerplane ($y = 0$) for $Re = 290$ and $x/D = 0$ to 5.6. Marked x/D locations correspond to PIV data in Fig. 9

vortex breakdown in the outlet channel, were numerically predicted in [27] for $Re \geq 180$. Importantly, the results of this study indicate that the transition point between these flow regimes is associated with the reemergence of flow symmetry, or a change from Fig. 5c to Fig. 5d, that negatively impacts mixing.

The Impact of Asymmetry

The topologies shown in Figs. 6 and 7 correspond to complex, three-dimensional vortex structures that extend into the outlet channel and significantly impact mixing. To illuminate the impact of asymmetry, consider Figs. 9 and 11, which display time-averaged PIV data in three planes for asymmetric and symmetric flow, respectively, and Figs. 10 and 12, which display corresponding flow fields in the outlet channel midplane ($x-z$ plane at $y = 0$, see Fig. 2.)

As shown in Fig. 9, asymmetric flow is characterized by significant entanglement of right and left incoming fluid streamlines in the corotating vortex structure. Streamlines entering the junction from the left, for example, (see Fig. 9, $x/D = 0$, streamlines originating from $-0.25 \leq y/D \leq 0$ at the left boundary) cross $z/D = 0$ to participate in the right vortex. As flow moves down the channel, from $x/D = 0$ to 1.175 in Fig. 9, increasing amounts of near-wall rightward and leftward streamlines cross the vertical centerline to participate in oppositely-located vortices, and by $x/D = 1.175$, the

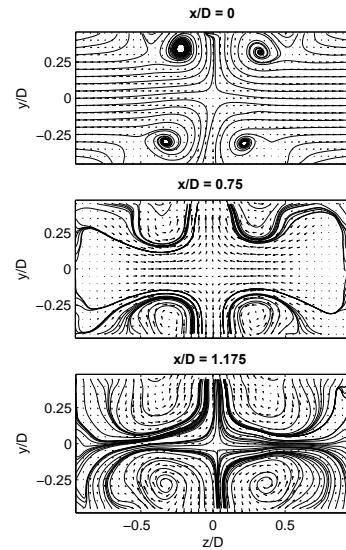


FIGURE 11. Time-averaged vector fields and streamlines for symmetric four-vortex flow in three viewing planes, $Re = 350$.

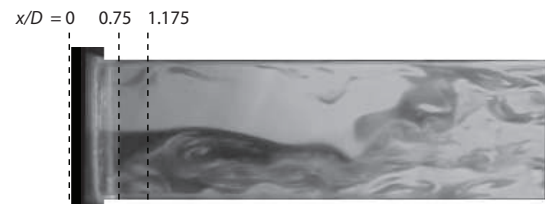


FIGURE 12. Instantaneous planar LIF image for unsteady symmetric flow in the outlet channel centerplane ($y = 0$) for $Re = 390$ and $x/D = 0$ to 5.6. Marked x/D locations correspond to PIV data in Fig. 11

right vortex consists of significant amounts of left-inlet fluid, and vice-versa. In contrast, unsteady symmetric flows in Fig. 11 are characterized, for time-averaged data in all three planes, by a symmetric four-vortex structure that separates right and left incoming flows.

The impact of asymmetry on the concentration distribution in the outlet channel is dramatic, as Figs. 10 and 12 indicate. Entanglement of oppositely dyed streamlines in an asymmetric vortex structure (Fig. 9) results in an outlet flow field with small scalar length scales, and substantial redistribution of incoming concentration, Fig. 10. Significant amounts of high-concentration fluid, which has entered the left inlet, or the top of Fig. 10, are now visible on the right side, or bottom half of Fig. 10, of the outlet channel, and vice-versa. The outlet channel flow field in Fig. 12 is significantly more segregated about the outlet channel centerline. Spanwise advection in the outlet channel in Fig. 12 is insufficient, in the absence of asymmetry, to mix incoming flows.

Outlet Channel Flow Fields

Outlet channel flow fields are presented in Fig. 13 for all flow regimes, and reveal the effect of flow structure in the T-channel junction on mixing to greater than 20 diameters downstream. Symmetric flows shown in Fig. 13a and d are visually segregated

throughout the interrogation region; in (a), diffusion occurs only at the central interface, in (b), spanwise advection has redistributed some incoming fluid, but large homogenous blobs, upon which diffusion cannot readily act, are still apparent in the flow field. Unstable stagnation points (Figs. 7 and 8) have resulted in limited streamline entanglement of oppositely-dyed fluid in outlet channel corner vortices (beginning near $x/D = 1.5$ and extending to $x/D = 2.5$ in Fig. 13d), but this is not widespread. Flow structures in Fig. 13d are largely convected for $x/D \geq 5.5$.

Asymmetric flow fields in Figs. 13b and c are characterized by smaller scalar structures, greater redistribution of incoming concentration, and qualitatively well-mixed flow fields by $x/D = 20.5$. Fig. 13b is especially revealing, and fine lamellar structures previously unresolved in the literature are visible. Vortical structures visible at $x/D = 1.5$ correspond to the asymmetric co-rotating vortex pair (Fig. 5b) that extends into the outlet channel and defines a highly rotational region. An additional large vortex pair described in [23] is visible in Fig. 13b beginning upstream of $x/D = 3.5$ and extending to $x/D = 5.5$. From Fig. 13b, the co-rotating vortex pair has the most significant impact on concentration redistribution, and flow structures appear largely convected for $x/D \geq 5.5$.

To quantify the impact of asymmetry on scalar length scales, non-dimensional concentration profiles $c(z/D)$ (extracted from Fig. 13 at discrete x/D locations) are shown in Fig. 14. Fourier transforms $X(k)$ of non-dimensional concentration profiles are shown in Fig. 15. Wavenumbers k correspond to flow length scales; incoming scalar length scales are of magnitude D and correspond, in Fig. 15, to wavenumber component $k = 2$ (or equivalently to a wavelength that is one-half of the outlet channel width of $2D$). As shown in Fig. 13, concentration length scales are significantly reduced with asymmetric flow. Spectra shown in Fig. 15 for $Re = 310$ and $Re = 220$, for unsteady and steady asymmetric flow respectively, contain significant high-wavenumber components that are more rapidly homogenized by diffusion. Far less length scale redistribution is present in the spectra for $Re = 400$ and $Re = 105$ in Fig. 15, for unsteady and steady symmetric flow respectively, where the initial scalar length scale is still visible in the $X(k)$ spike at $k = 2$.

Importantly, length scales associated with steady and unsteady asymmetric flows (Figs. 15 b and c) are similar for all x/D locations, which suggests that advective mixing in the outlet channel does not significantly reduce incoming length scales. This is also indicated by Figs. 13b (steady) and c (unsteady), which have qualitatively similar concentration distributions and appear equally well mixed at $x/D \geq 20.5$. Hence, similar mixing behaviors (accounting for different residence times with higher and lower flow rates) might be expected for steady and unsteady asymmetric flows. Thus, primary consideration should be given to maintaining an asymmetric momentum field, whether flows are steady or not.

Length scales in Fig. 15 can also be used to assess expected mixing increases for asymmetric vs. symmetric flow regimes. To quantify mixing improvement, an expression for non-dimensional mixing length $(x/D)_m$ can be written, for flows where mixing occurs purely by diffusion, as [29]:

$$(x/D)_m \sim Pe \times l/D \quad (1)$$

where l the characteristic length or striation thickness over which diffusion must occur, D is the inlet channel diameter, and Pe is the Peclet number, equivalently $Re \times Sc$. For symmetric flow, dominant length scale $l \approx D$ in the outlet channel (Fig. 15, $Re = 105$), and from Eqn. 1

$$(x/D)_m \sim Pe \quad (2)$$

For asymmetric flow, incoming length scale D is significantly reduced such that, by the end of stirring region $x/D \leq 5.5$, beyond which flows appear largely convected, dominant length scale $l \approx D/3$ (Fig. 15, $Re = 220$). Hence, for asymmetric flows, Eqn. 1 becomes

$$(x/D)_m \sim Pe/3 \quad (3)$$

Dependence of mixing length on Pe in Eqns. 2 and 3 is linear and suggests a three-fold reduction in mixing length $(x/D)_m$ with asymmetric flow. Bear in mind that this is based only on length scale characterizations in the outlet channel centerplane; a three- to sixfold increase in mixing quality was predicted in the literature [21, 22, 25, 26] based on overall mixedness at the outlet.

Reduced scalar length scales are beneficial to mixing, but it should be recognized that, while momentum fields are equivalent for geometrically and dynamically similar T-channels, the overall mixedness of flow fields shown in Fig. 13 will vary with size and Sc . Thus, scalar length scales in Fig. 14 and Fig. 15 will be of similar magnitude relative to integral length scale D for smaller T-channels, but significantly smaller in absolute scale and thus more readily diffused. There is no loss of generality in such a fundamental approach, as the goal of this paper is to provide a detailed look at flow structure rather than to present mixing characterizations. Intuitively, any departure from conventional theory and boundary conditions may also limit the applicability of the present study. Roughness elements, which affect transport processes near the wall and are increasingly non-negligible as surface-to-volume ratio decreases, are of particular concern on the microscale, and T-channels with significant surface roughness may be geometrically and behaviorally dissimilar from the present study. A good review of roughness and MEMS is given in [30].

Periodicity and Mixing Impacts

Outlet flow fields for unsteady flow regimes (Figs. 13c and d) are periodic, as indicated by point-LIF data at six discrete downstream x/D locations in the outlet channel centerline, shown in Fig. 16, for unsteady asymmetric flows (a) and unsteady symmetric flows (b). Waveform time periods visible in Fig. 16 correspond to the oscillatory processes (Figs. 6 and 7) occurring in the junction.

To quantify periodicity in the present study, autocorrelation functions $R(\tau)$, where τ is an applied lag time, were computed for point-LIF waveforms at $x/D = 1.5$ for all unsteady flows. Periodic $R(\tau)$ that are significantly nonzero for all lag times indicate repeating flow structure. An average autocorrelation value \bar{R} was additionally computed for discrete Re ranges by 1) extracting the average magnitude of all positive correlation peaks for each periodic

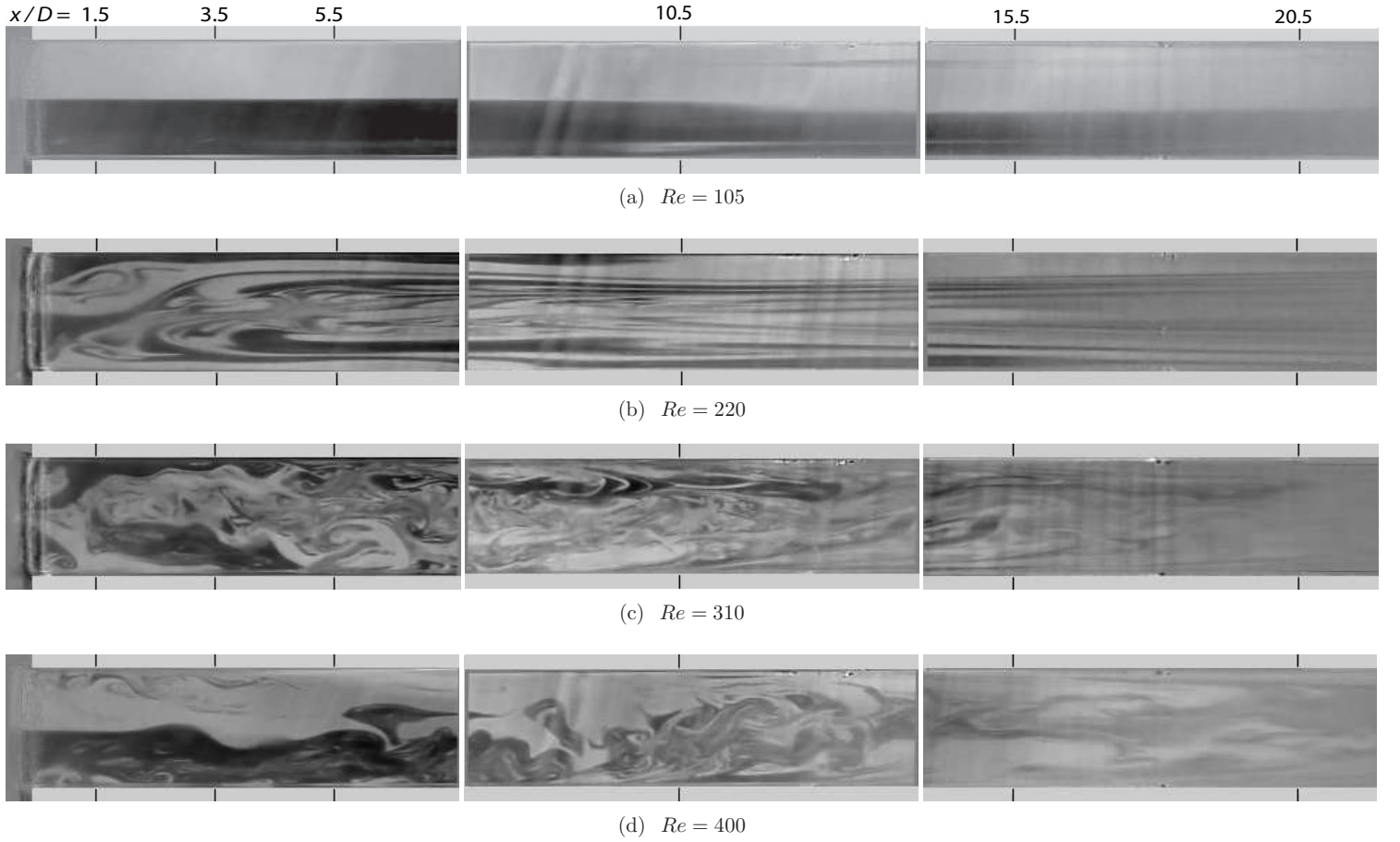


FIGURE 13. Planar LIF results in the outlet channel for (a) steady symmetric flow at low Re , (b) steady asymmetric flow, (c) unsteady asymmetric flow, and (d) unsteady symmetric flow at higher Re . Tick marks delineate photodetector locations. Doped fluid is entering from the top in each figure.

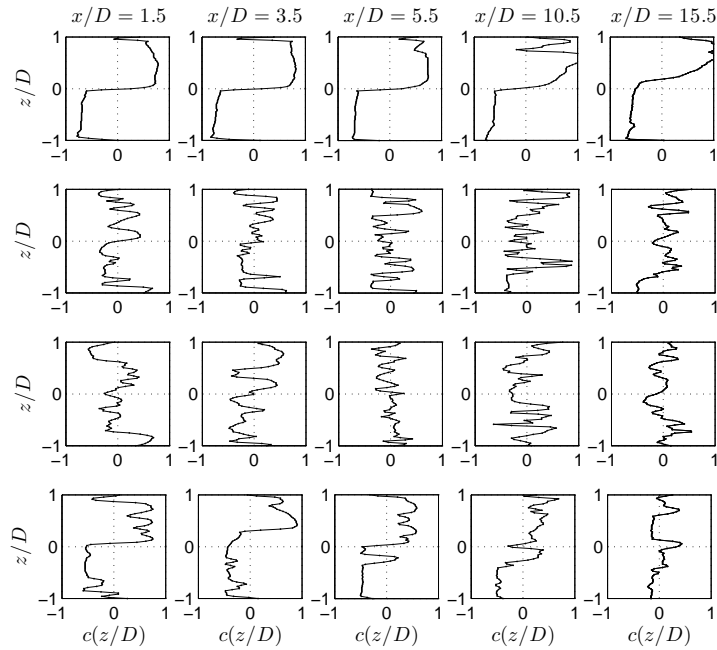


FIGURE 14. Concentration profiles for $Re = 105, 220, 310$ and 400 (top to bottom) extracted from the scalar concentration fields shown in Fig. 13

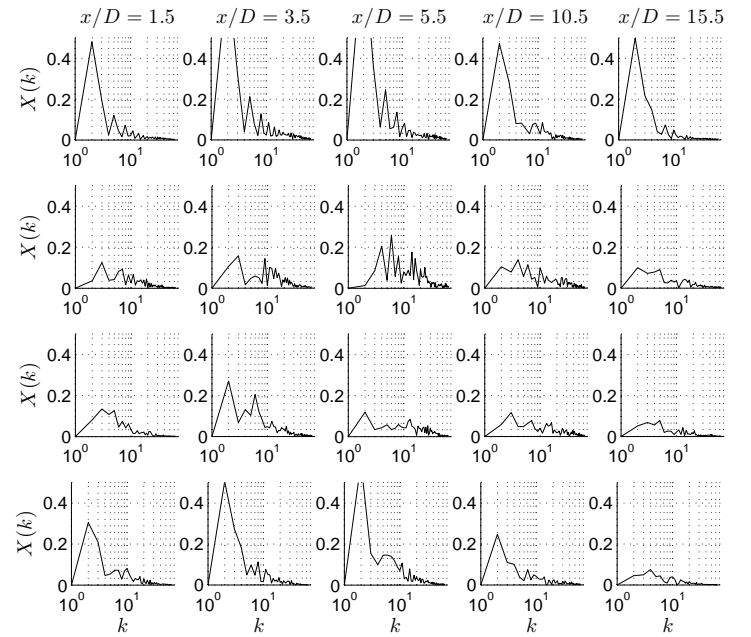


FIGURE 15. Wavenumber spectra for $Re = 105, 220, 310$ and 400 (top to bottom) extracted from the scalar concentration fields shown in Fig. 13

TABLE 1. Periodicity of data, as indicated by the percentage of periodic autocorrelation functions $R(\tau)$ observed for each Re range. The average correlation \bar{R} is also shown. Waveforms associated with scalar concentration at $x/D = 1.5$ are used to calculate $R(\tau)$ and \bar{R} .

Re Range	% Periodic $R(\tau)$	\bar{R}
200-249	100	0.59
250-299	100	0.35
300-349	92	0.30
350-399	75	0.23
400-422	50	0.18

$R(\tau)$ and Re , and 2) averaging the results. Note that high values of \bar{R} indicate that structures in the outlet channel are more precisely repeated. The percentage of periodic $R(\tau)$ and average correlation \bar{R} are presented in Table 1 for discrete Re ranges.

Results in Table 1 suggest that, as predicted in [27], flows for $Re < 300$ are strictly periodic. For $300 < Re < 399$, flows are increasingly aperiodic, and a decline in \bar{R} indicates that flow structures are less perfectly repeated. Again, these data align with predictions of quasi-periodic flow for $300 < Re < 375$ [27]. Importantly, flows for $Re \geq 400$ are greater than 50% aperiodic, which aligns well with numerical predictions of chaotic-laminar flows for $Re > 375$ [27]. Identification of this transition point is especially important, as the wide spread of mixing qualities predicted in [27] suggest that the onset of chaotic laminar flow is at best, not beneficial to mixing, and at worst, highly detrimental, decreasing mixing quality by (qualitatively) 75%.

DNS results in [27] identified the quasi-periodic flow that occurs at higher Re ($300 < Re < 375$) as characterized by bursts of increased mixing quality followed by breakdowns to a lower mixing quality. This behavior is consistent with periodic transitions to an asymmetrical flow field observed in the present study for unsteady four-vortex flows (Fig. 7 and Fig. 13d). At higher Re , symmetry is generally persistent, as LIF results in Fig. 7 indicate, but mixing improves when periodic breaks from symmetry occur, and the outlet channel flow field transitions from that shown in Fig. 13d to that shown in Fig. 13c. Breaks to asymmetric flow likely correspond to the burst of improved mixing predicted in [27] and subsequent breakdowns in mixing quality occur when the flow returns to an oscillatory four-vortex state. Because breaks from symmetry, and the resultant burst of improved mixing quality, are temporary and unpredictable, operation in the unsteady symmetric range is not recommended. Further characterization of oscillatory behaviors and associated time scales can be found in Thomas *et al.* [31,32].

The Regime Map

PIV and LIF trials in Table 2 were used to generate the regime map shown in Fig. 17. For each discrete Re in Fig. 17, the number of occurrences of a symmetric topology n_s is normalized by N total experimental trials at that Re . n_s includes steady stagnation and four-vortex flows at low Re , and unsteady symmetric flows at

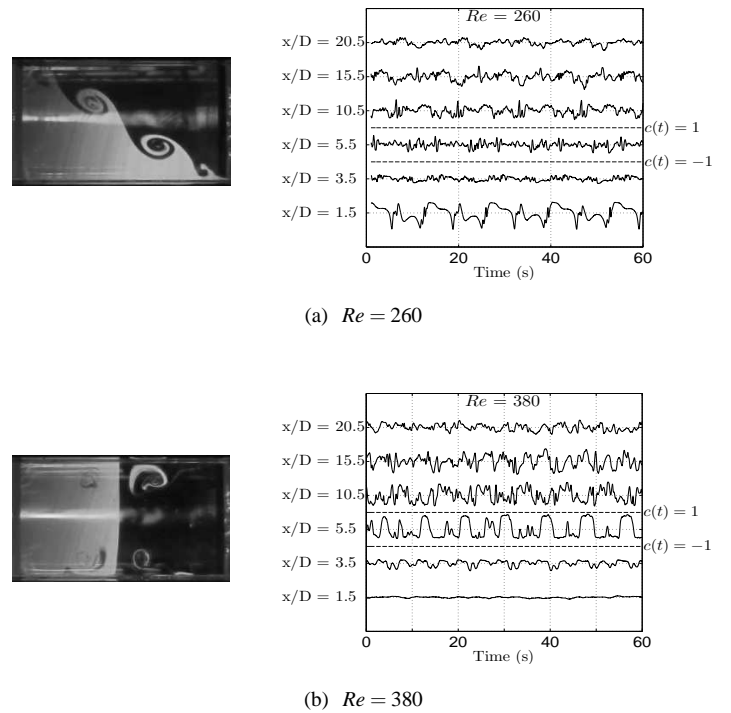


FIGURE 16. Simultaneous planar-LIF in the T-junction (left) and point-LIF in the outlet channel (right) for a) unsteady asymmetric flow and b) unsteady symmetric flow. A 60 s interval is shown for point-LIF data. Voltage signals have been scaled to represent concentration $c(t)$ in the centerline, which varies from $c(t) = 1$ (for high concentration fluid) to $c(t) = -1$ (for clear fluid). Scale is indicated for the photodetector located at $x/D = 5.5$. LIF images for each Re were extracted at $t = 0$.

TABLE 2. Cumulative PIV and LIF Trials used to generate the Regime Map (Fig. 17)

Re Range	Cumulative Trials (N)
422-373	5
398-335	5
354-277	7
293-218	7
212-131	10
141-56	6

higher Re . Occurrences of asymmetric flow are represented by $1 - n_s$.

Fig. 17 indicates some overlap in flow regimes, which are also broadly defined in the literature. For $Re \leq 116$, flows are steady and symmetric, and stagnation-point flow (at the lowest Re) and four-vortex flows are dominant. For $68 \leq Re \leq 141$, both symmetric and asymmetric flows were observed; in one of six trials at the lowest flow rate, a steady two-vortex topology persisted until $Re = 68$. For $142 \leq Re \leq 298$, flow is almost exclusively asymmetric. A transition to asymmetric flow near $Re = 142$ is

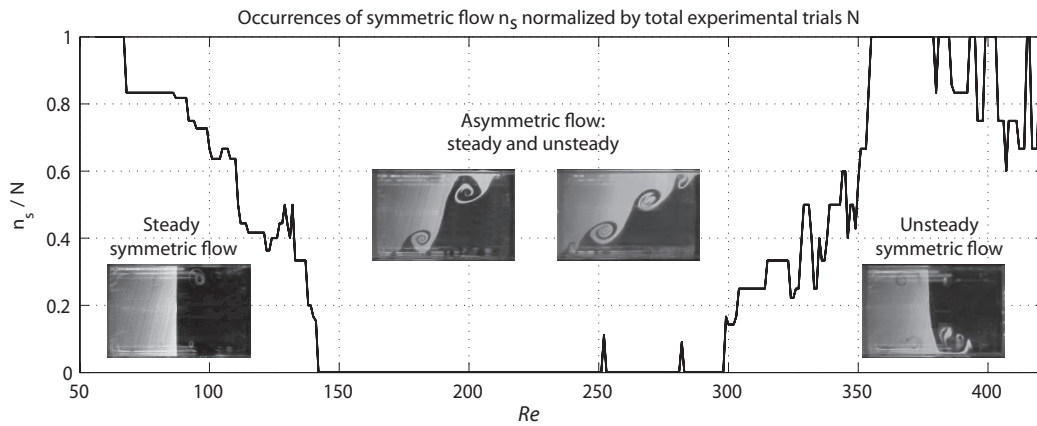


FIGURE 17. Regime map for all PIV and LIF trials; occurrences of symmetric flow n_s are normalized by total trials N for each Re . $1 - n_s$ represents the occurrence of asymmetric flow, and both regimes are labeled in the figure. At lower Re , symmetric flow includes steady stagnation-point and four-vortex flow, and at higher Re , flows are symmetrical but unsteady. Asymmetric flow includes both unsteady shear-layer flow and steady asymmetric flow.

supported in the literature [21, 22, 33]. Asymmetric flows for $195 \leq Re \leq 298$ are generally unsteady. For Re between 335 and 350, flows regain a degree of symmetry. Periodic breaks from symmetry occur in this regime, as indicated in Fig. 17, which are more frequent with increasing Re .

Importantly, the regime map indicates that asymmetric flow, which is positively indicated for mixing, occurs almost exclusively, based on five or more trials for each discrete Re (Table 2), for a moderate Re range of $142 \leq Re \leq 298$. Therefore, this is the recommended operating range.

CONCLUSIONS

An experimental study of water flow in a T-shaped channel with rectangular cross section has been presented for a Reynolds number range of 56 to 422. Dynamical conditions and T-channel geometry of the current study are applicable to the microscale, and experimental results support a large body of numerical work. Lower Re flow regimes predicted in the literature were experimentally confirmed, and unsteady mixing regimes that occur at higher Re were experimentally characterized for the first time. Unsteady behaviors include an asymmetric, corotating two-vortex structure that exhibits periodic shear-layer roll up behavior in the T-channel junction, and a symmetrical four-vortex flow for $Re \geq 350$ that appears detrimental to mixing. Symmetrical flows for $Re \geq 350$ exhibit quasi-periodic behavior when breaks from symmetry, which are not predictable, arise from unstable stagnation point oscillation in the T-channel junction. These temporary transitions to an asymmetric momentum field are likely associated with the burst of improved mixing predicted in the literature; a subsequent decay in mixing quality occurs when the oscillatory four-vortex state is resumed. The impact of asymmetry on outlet channel flow fields is dramatic, whether flows are steady or not. An asymmetric corotating vortex structure, which leads to extensive streamline entanglement and deformation, results in significant redistribution of incoming concentration and reduction of incoming scalar length scales in the outlet channel. Improvements in mixing are therefore expected for asymmetric flows. Importantly, flows for $142 \leq Re \leq 298$ were exclu-

sively asymmetric, based on multiple experimental trials; thus, this is the recommended operating range.

ACKNOWLEDGMENT

Many thanks to the National Science Foundation Integrated Graduate Education Research and Training (IGERT) program, whose financial support has made this research possible.

REFERENCES

- [1] McDonald, J. C., Metallo, S., and Whitesides, G., 2001. "Fabrication of a configurable, single-use microfluidic device". *Analytical Chemistry*, **73**, pp. 5645–5650.
- [2] Reyes, D., Iossifidis, D., Auroux, P.-A., and Manz, A., 2002. "Micro total analysis systems. 1. introduction, theory, and technology". *Analytical Chemistry*, **74**, pp. 2623–2636.
- [3] Erickson, D., and Li, D., 2004. "Integrated microfluidic devices". *Analytica Chimica Acta*, **507**, pp. 11–26.
- [4] Ashley, S., 1997. "Turbines on a dime". *Mechanical Engineering-CIME*, pp. 78–81.
- [5] Fichtner, M., Brandner, J., Linder, G., Schygulla, U., Wenka, A., and Schubert, K., 2001. "Microstructure devices for applications in thermal and chemical process engineering". *Microscale Thermophysical Engineering*, **5**(1), pp. 17–39.
- [6] Nakajima, N., Ogawa, K., and Fujimasa, I., 1989. "Study on microengines: Miniaturizing stirling engines for actuators". *Sensors and Actuators*, **20**, pp. 75–82.
- [7] Darabi, J., and Ekula, K., 2003. "Development of a chip-integrated micro cooling device". *Microelectronics Journal*, **34**, pp. 1067–1074.
- [8] Karniadakis, G. E., and Beskok, A., 2002. *Micro Flows, Fundamentals and Simulation*. Springer-Verlag, Berlin.
- [9] Ho, C.-M., and Tai, Y.-C., 1998. "Micro-electro-mechanical systems (mems) and fluid flows". *Annual Review of Fluid Mechanics*, **30**, pp. 579–612.
- [10] Nguyen, N.-T., 2005. "Micromixers, a review". *J. Micromech. Microeng.*, **15**, pp. 1–15.

- [11] Mitchell, P., 2001. "Microfluidics: downsizing large-scale biology". *Nature Biotechnology*, **19**, pp. 717–721.
- [12] Deval, J., Tabeling, P., and Ho, C.-H., 2002. "A dielectrophoretic chaotic mixer". *Proceedings of the 15th IEEE international conference on micro electro mechanical systems*, pp. 36–39.
- [13] Suzuki, H., and Ho, C.-M., 2002. "A magnetic force driven chaotic micro-mixer". *Proceedings of the 15th IEEE international conference on micro electro mechanical systems*, pp. 40–43.
- [14] Leu, T.-S., and Ma, F.-C., 2005. "Novel ehd-pump driven micro mixers". *Journal of Mechanics*, **21**(3), pp. 137–144.
- [15] Koch, M., Chatelain, D., Evans, A., and Brunnschweiler, A., 1998. "Two simple micromixers based on silicon". *Journal of Micromechanics and Microengineering*, **8**(2), pp. 123–126.
- [16] Branebjerg, J., Gravesen, P., Krog, J., and Nielsen, C., 1996. "Fast mixing by lamination". *Proceedings of the ninth annual IEEE international workshop on micro electro mechanical systems*, pp. 441–445.
- [17] Miyake, R., Lammerink, T., Elwenspoek, M., and Fluitman, J., 1993. "Micro mixer with fast diffusion". *Proceedings of IEEE MEMS '93: An Investigation of Micro Structures, Sensors, Actuators, Machines and Systems*, pp. 248–253.
- [18] Ehlers, S., Elgeti, K., Menzel, T., and Wiebmeier, G., 2000. "Mixing in the offstream of a microchannel system". *Chemical Engineering and Processing*, **39**, pp. 291–298.
- [19] Bertsch, A., Heimgartner, S., Cousseau, P., and Renaud, P., 2001. "3d micromixers - downscaling large scale industrial static mixers". *Proceedings of the 14th IEEE international conference on micro electro mechanical systems*, pp. 507–510.
- [20] Perkins, J., Stephanoff, K., and Murray, B., 1989. "Mixing enhancement in flow past rectangular cavities as a result of periodically pulsed fluid motion". *IEEE Transactions on Components, Hybrids and Manufacturing Technology*, **12**(4).
- [21] Kockmann, N., Foll, C., and Woias, P., 2003. "Flow regimes and mass transfer characteristics in static micro mixers". *Micromixers, BioMEMS and Medical Microsystems, Proceedings of SPIE*, **4982**, pp. 319–329.
- [22] Engler, M., Kockmann, N., Kiefer, T., and Woias, P., 2004. "Numerical and experimental investigations of liquid mixing in static micromixers". *Chemical Engineering Journal*, **101**, pp. 315–322.
- [23] Kockmann, N., Kiefer, T., Engler, M., and Woias, P., 2006. "Convective mixing and chemical reactions in microchannels with high flow rates". *Sensors and Actuators B*, **117**(2), pp. 495–508.
- [24] Wong, S., Ward, M., and Wharton, C., 2004. "Micro t-mixer as a rapid mixing micromixer". *Sensors and Actuators B*, **100**, pp. 359–379.
- [25] Hoffmann, M., Schluter, M., and Rabiger, N., 2006. "Experimental investigation of liquid-liquid mixing in t-shaped micro-mixers using micro-lif and micro-piv". *Chemical Engineering Science*, **61**, pp. 2968–2976.
- [26] Bothe, D., Stemich, C., and Warnecke, H.-J., 2006. "Fluid mixing in a t-shaped micro-mixer". *Chemical Engineering Science*, **61**, pp. 2950–2958.
- [27] Dreher, S., Kockmann, N., and Woias, P., 2009. "Characterization of laminar transient flow regimes and mixing in t-shaped micromixers". *Heat Transfer Engineering*, **30**(1–2), pp. 91–100.
- [28] Telib, H., Manhart, M., and Iollo, A., 2004. "Characterization of laminar transient flow regimes and mixing in t-shaped micromixers". *Physics of Fluids*, **16**(8), pp. 2717–2731.
- [29] Stroock, A., Dertinger, S., Ajdari, A., Mezic, I., Stone, H., and Whitesides, G., 2002. "Chaotic mixer for microchannels". *Science*, **295**, pp. 647–651.
- [30] Kandlikar, S., 2008. "Exploring roughness effect on laminar internal flow—are we ready for change?". *Nanoscale and Microscale Thermophysical Engineering*, **12**(1), pp. 61–82.
- [31] Thomas, S., Ameal, T., and Guilkey, J., 2010. "Mixing kinematics of moderate reynolds number flows in a t-channel". *Physics of Fluids*, **22**(013601).
- [32] Thomas, S., and Ameal, T., 2010. "An experimental investigation of moderate reynolds number flow in a t-channel". *Experiments in Fluids*, DOI: 10.1007/s00348-010-0863-7.
- [33] Kockmann, N., Engler, M., Foll, C., and Woias, P., 2003. "Liquid mixing in static micro mixers with various cross sections". In *Proceedings of the First International Conference on Microchannels and Minichannels*, Vol. 14, pp. 114–121.